ORIGINAL PAPER

Fabric evolution and strain localisation in inherently anisotropic specimens of anisometric particles (lentils) under triaxial compression

Gustavo Pinzón[1] · Edward Andò[2] · Jacques Desrues[1] · Gioacchino Viggiani[1]

Abstract

Inherent anisotropy is often observed in natural soils and other granular materials formed during gravity deposition. Fabric characterisation and evolution have been mainly studied using numerical simulations, given the difficulty of retrieving the contact network and the kinematics of particles in physical experiments. This work presents the results of five triaxial compression tests on inherently anisotropic lentil specimens imaged with x-ray tomography. Each specimen is prepared in a way such that all the particles present a unique mean orientation, as results from gravity in natural soils deposits - this can be called "bedding effect". Particles are identified and tracked from the first image all the way through the test using a novel tracking algorithm, enabling the measurement of particle and contact fabric evolution, as well as strain localisation within the specimens. The results reveal that the deformation processes take place essentially in a planar scenario, both at a micro and mesoscale. Additionally, it is observed that under deviatoric loading two mechanisms are responsible for fabric evolution: rotation of the main orientation of the fabric tensor, and increase of the anisotropy. Finally, the orientation of the shear band is found to be independent of the initial orientation of the particles.

Keywords Anisometric particles · Inherent anisotropy · Fabric · Lab testing · X-ray tomography

1 Introduction

Natural soil deposits result frequently from a steady deposition process under gravity. This deposition process generates an inherent structural anisotropy (*i.e.* the orientation of particles, the orientation of contacts) inside the material, prior to any loading process. This inherently anisotropic granular array has a unique arrangement of the internal structure (or fabric), that characterises the initial state and directly affects the mechanical response of the specimen. Anisotropy at the macro scale is strongly affected by the particle scale - specially their shapes: a deposit of isometric particles (sphere) results in a more homogeneous distribution of the contact network than gravity deposition of anisometric particles (ellipsoids), where a strong principal direction

of the contact network is obtained. The understanding of the link between the macroscopic behaviour and the evolution of fabric anisotropy lies at the core of the mechanics of granular media, considering that when a granular material is subjected to shear, particle rearrangement takes place together with the creation/loss of contact between particles. Early experimental efforts in understanding the effect of inherently anisotropic fabric were performed by [1], who subjected cubical specimens of rounded Leighton Buzzard sand to triaxial compression, and showed a difference in the drained strength response for specimens with different deposition planes. Similarly [2] tested several types of sands under triaxial conditions. The results obtained through the preparation of thin sections and optical microscopy measure, for the first time, the initial state of particle-based and contact normal-based fabric in granular materials. A clear alignment of the particles and the contact network with the vertical axis is observed for all the materials, and the intensity of the anisotropy is related to the flatness or elongation of the particles. Further studies used plane strain conditions [3, 4] and reproduced the result on strength anisotropy, additionally presenting the first results on the inclination of the shear bands for inherently anisotropic specimens. Moreover,

✉ Gustavo Pinzón
gustavo.pinzon@3sr-grenoble.fr

1   Université Grenoble Alpes, CNRS, Grenoble INP, 3SR, F-38000 Grenoble, France

2   Present Address: EPFL Center for Imaging, École Polytechnique Fédérale de Lausanne (EPFL), Lausanne, Switzerland

[5] presented the first study where the shape and friction of the particles were controlled, by performing a biaxial compression test on oval cross-section rods with two values of aspect ratio and inter-particle friction. The results revealed that contacts between particles tend to be generated along the direction of the major principal stress, while a greater aspect ratio of the particles increased the strength anisotropy between the specimens. Additional studies focused on the effect of the intermediate principal stress [6, 7] on the volumetric behaviour of the material, and the shear strength of the material. The authors showed that the minimum value of shear strength is achieved when the maximum stress obliquity plane is parallel to the bedding plane. The latest physical experiments performed on inherently anisotropic specimens were focused on strain localisation [8, 9]. The authors showed that two types of shear bands are kinematically possible regarding their orientation relative to the bedding plane orientation: Type-A if the shear band is perpendicular to the bedding plane, or Type-B if both orientations are parallel. Additionally, the inclination of the observed shear bands was measured between the zero-extension direction (Roscoe rupture plane) and the maximum stress obliquity (Coulomb rupture plane).

The use of numerical techniques such as the discrete element method (DEM) provides the opportunity to evaluate quantities at the particle scale level, measure the evolution of fabric with ease, and perform parametric studies under controlled conditions. Several researchers [10–13] used 2D simulations on oval/elongated particles to study the effect of inherent anisotropy on the evolution of fabric and the macroscopic response of granular materials. The results revealed a difference between the macroscopic strength and volumetric response of specimens with different initial orientations, as observed in previous experimental studies. The authors showed that the evolution of fabric is dependent on the initial orientation of the specimen but, when subjected to large deformations, they all converge to a unique state in terms of orientation and anisotropy. One of the major contributions was made by [14], focusing on the origins of shear strength of inherently anisotropic materials from a micromechanical perspective. In their study, the authors prove that the shear strength is not the same along different planes for specimens with inherent anisotropy (which contravenes one of the primary assumptions of the Mohr-Coulomb criterion), thus the mechanical resistance of this type of materials must be understood in terms of the inclination of the bedding plane with respect to a potential shear plane. Employing 2D simulations of direct shear on ellipses, a shear failure criterion was determined as a function of the inclination angle and the results were validated through the results obtained from biaxial compression tests. Surprisingly, failure does not occur along the maximum obliquity plane, nor

a direction parallel to the bedding plane, but rather at a plane that reaches its local shear strength sooner.

Further DEM studies focused on the effect of the bedding plane on strain localisation. 2D FEM-DEM simulations were performed by [15], and demonstrated that the orientation of the bedding plane is not necessarily the "weakest" direction for the shear band to develop, while the asynchronous evolution of the particle-based and contact normal-based fabric plays a role on the triggering of strain localisation. On the other hand, [16] performed 2D and 3D DEM biaxial/triaxial compression test on ellipses/ellipsoids focusing on dilatancy. The results show that it is not only dependent on the initial fabric anisotropy, but is also influenced by the evolution of fabric, especially the contact normal fabric. At low values of deviatoric stress ratio under biaxial and triaxial loading, differences in the initial fabric anisotropy of granular materials can lead to distinctly different dilatancy ratios. However, as loading continues, the deviatoric stress ratio, void ratio, and fabric of granular materials evolve toward a unique critical state, causing the dilatancy ratio to converge irrespective of its initial value. The latter means that the anisotropic critical state theory (ACST), presented in [17] as an extension of classical critical state theory including the role of fabric, is capable of providing a framework for the quantitative mathematical depiction of the dependency of dilatancy ratio on fabric anisotropy.

Within 3D physical experiments, it is almost impossible to quantify fabric evolution along the test without direct imaging, and this reflects on the fact that, to the best of the authors knowledge, almost 30 years have passed since the last physical experiments on inherently anisotropic materials. For that reason, *in-operando* x-ray tomography imaging can be considered as an ideal tool to measure and follow the evolution of the material fabric for the first time, since it enables the generation of a complete 3D reconstruction of the specimen. Given that individual grains can be identified, particle-based fabric can be retrieved with ease, while the measurement of inter-particle contact fabric presents unique challenges that emerge from the complexity of contact detection on x-ray images. A methodology to address the latter challenge is presented and discussed in [18]. Additionally, the kinematics of individual grains can be tracked during the test, offering the possibility to compute strain fields inside the specimen and examine strain localisation patterns. The present study aims to present the effect of inherent anisotropy on the evolution of the contact fabric, making use of x-ray tomography to image five specimens comprising approximately 9000 lentils during triaxial compression. The anisometry of lentils guarantee that the initial fabric presents a strong anisotropy towards a preferential orientation. The specimens are prepared with particles oriented at a specific bedding angle with respect to the loading axis, and the effect of inherent anisotropy is observed in

the evolution of particle-based and contact normal-based fabric. Special attention is given to the mechanisms that allow the fabric re-alignment towards the direction of the major principal stress. In addition, the characteristics and evolution of strain localisation and its relation to the bedding angle of the specimen are presented and discussed. All the data used and presented in this work is available in an open repository [19].

The outline of the paper is as follows. In Sect. 2 the properties of the tested materials are presented, along with the experimental conditions used. A detailed description of the image analysis techniques is given, as well as the novel particle tracking methodology implemented. In Sect. 3 the experimental results are shown, inclusing the macroscopic response and definition of the study region, the grain kinematics and the evolution of fabric. Special attention is given to the deviatoric strain fields and the presence of strain localisation. Section 4 discusses the contributions and further studies on this topic.
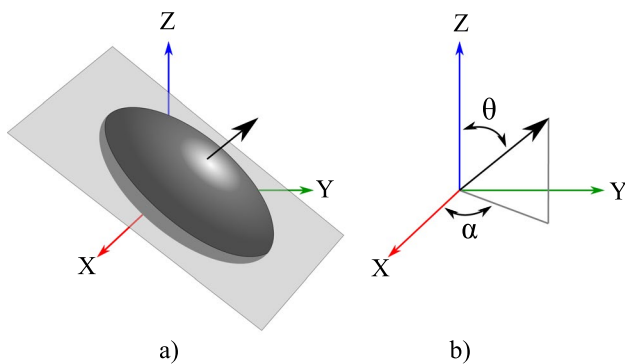
Fig. 1 Coordinate system: **a** plane of symmetry of a lentil; **b** decomposition of the orientation vector into its inclination (θ) and azimuth (α) in the XYZ reference frame

2 Material & methods

2.1 Material and experiments

In this study five triaxial compression tests at 50 kPa confining pressure were performed on cylindrical specimens of $\approx$140mm height and $\approx$70mm diameter. The end caps are frictional and cannot move in the horizontal plane nor rotate. Each specimen is composed of more than 9000 dry natural green lentils, that can be approximately described mathematically as oblate ellipsoids with a long axis of $\approx$4.6mm $\pm$0.3mm, and a short axis of $\approx$2.6mm $\pm$0.1mm, yielding an aspect ratio of 1.8 $\pm$0.2. Particles are characterised by a plane of symmetry, and the vector normal to this plane will be used to describe the orientation of each particle in space. Each orientation vector is decomposed into an orthogonal coordinate system described by its inclination (θ), and azimuth (α) (Fig. 1). The strong anisometry of lentils ensures that, when deposited, they tend to arrange with their orientation vector parallel to gravity yielding a strongly anisotropic arrangement. This is exploited to create the specimens at any desired orientation by simply tilting the mould with the stretched membrane at the target angle (with respect to the vertical axis).

The lentils are then spooned manually until the mould is filled, the end cap is placed, and vacuum is applied to the specimen. The external mould is removed and the specimen is placed inside the triaxial compression cell. The low confinement generated by the vaccum assures that the particles do not break during the test. Figure 2 displays vertical greyscale slices at the middle of the specimen for all five specimens, before any deviatoric loading is applied.

X-ray tomography is used to scan the specimen at regular intervals of 1% axial shortening - halting the loading system during the scan. A voxel size of 180μm/vox is used to image
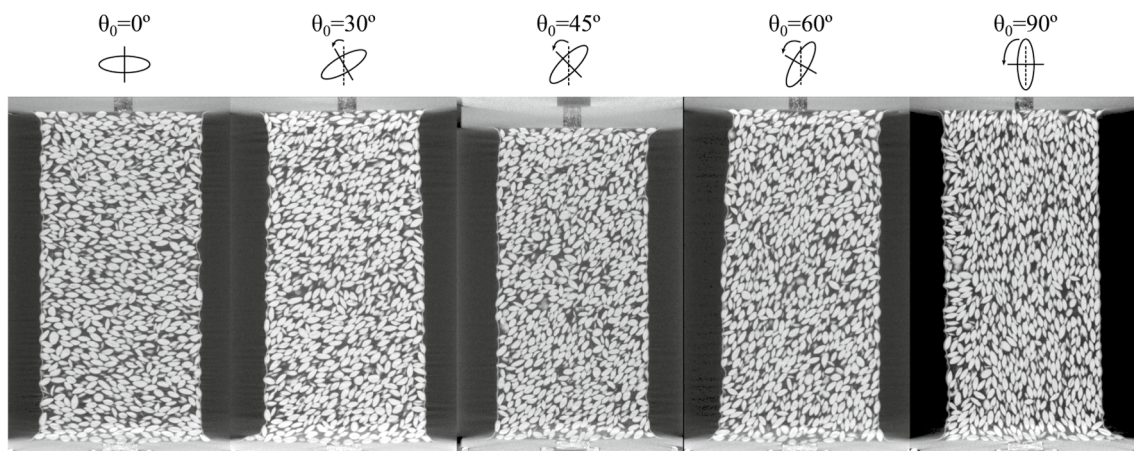
Fig. 2 Central vertical greyscale slices of the initial state of the five tested specimens

the specimen, resulting in 3D images of $600 \times 600 \times 850$ voxels. The only external measurement is the axial force and the displacement of the loading stage, while all the other quantities are measured directly from the 3D images. Table 1 presents a summary of the initial state of each test. Specimens are labelled as *LENGPXX*, where the last two digits correspond to the target orientation θ_0. Given that the shape of the particles can be described by ellipsoids, the maximum and minimum void ratios can be computed with ease, since both are functions of the excluded volume (v_{ex}) [20]. For an oblate ellipsoid with an aspect ratio $w < 1$, the latter is computed as $v_{ex} = 2 + (3/2)(1 + \frac{w^2}{e} tanh^{-1} e)(1 + \frac{1}{we} sin^{-1} e)$, with $e^2 = 1 - w^2$. Figure 2a of [20] is then used to compute the maximum (*i.e.* $\mu = \infty$) and minimum (*i.e.* $\mu = 0$) void ratio of the assembly. For the tested specimens, the relative density D_r ranges from 63% to 76%, which indicates that the preparation method enables the fabrication of specimens with limited variability of the initial void ratio.

2.2 Image analysis

The python-based open-source software *spam* [21] is used for image-analysis of each experiment. The 3D grey-scale image obtained from the initial scan is used to identify and label each particle. First, a morphological greyscale reconstruction [22] is applied in order to homogenise the greyscale distribution inside each phase (solid and void) while preserving the morphological features of the particles. Afterwards, a Laplace filter, using Gaussian second derivatives, is employed to reduce partial volume effect [23]. At this point the 16-bit greyscale histogram is normalised in order to have the void and solid phase peaks at 0.25 and 0.75, respectively. The solid and void phases are then separated using a normalised threshold of 0.5. The end caps and the membrane are removed from the obtained binary image, thresholding their greyscale value only around their zone of influence. The binary image is then fed to a watershed algorithm to identify and label each individual particle. A visual validation is performed, resorting in a manual post-processing procedure used to correct the segmentation errors, obtaining a "golden standard" initial labelled image - *i.e.*, a high-fidelity digital representation of the position and shape of the physical

Table 1 Initial conditions of all five specimens

Specimen	θ_0	Void ratio
LENGP00	1.3° (± 0.9°)	0.549
LENGP30	33.7° (± 0.9°)	0.555
LENGP45	46.1° (± 0.9°)	0.576
LENGP60	58.6° (± 0.9°)	0.539
LENGP90	89.5° (± 0.6°)	0.525

particles. This time-consuming procedure is only done for the first scan of each experiment.

The density of scans acquired during deviatoric loading (*i.e.*, performed at regular small intervals) facilitates the tracking of the particles since the displacement of the particles between two subsequent scans is quite small. The tracking is performed using a novel discrete digital image correlation technique (based on [24–26]), and uses a *total* approach, *i.e.*, following each particle between the reference state (initial scan) and a deformed state (scan *n*). Specifically, the tracking of an object consists in finding the transformation (Φ) that maps the variation between the greylevels of a reference state (*im1*) and an altered state (*im2*). If Φ is applied to the reference state and compared to the altered state (*i.e.*, $im1(\Phi) - im2$), the residual of the transformation should be zero. However the noise found inherently in x-ray tomography images impedes the residual to be 0, thus reducing the tracking to a minimisation problem - finding the transformation that minimises the residual. The latter is computed over a region that comprises the object in question, and for the case of single-particle tracking, the dilated labelled image of each particle is used to mask the greyscale region to be used. In order to facilitate the tracking of the particles, the transformation of each particle at state $n - 1$ is used as the initial guess for the tracking at the state n. Additionally, the initial guess of particles that do not converge at a given iteration is recomputed as the mean transformation of their direct neighbours. This enables the image correlation procedure to converge for *all* particles in *all* increments with relative ease.

Once all the particles are properly tracked between the reference state and a subsequent scan *n*, a deformed labelled image is generated by applying the measured linear transformation to each label, and the subsequently moved particle is used as a seed for segmenting the binary image of scan *n*. This generates a consistent labelling of the particles throughout the test, greatly facilitating analysis such as measuring the evolution of the contact network, in terms of creation, loss, and preservion of contacts (see [27]).

The labelled images, along with the tracking results, are used to describe the overall deformation as well as the strain field in the specimen. The macroscopic axial shortening (ϵ_a) and the volumetric strain (ϵ_v) are measured directly from each scan employing binary filled images, obtained through a series of consecutive binary erosions and dilations applied over the solid phase (as proposed in [28]). The axial shortening is defined as $\epsilon_a = (L_0 - L_i)/L_0$, where L_0 and L_i are the height of the binary filled image at the initial and deformed state, respectively. Similarly, the macroscopic volumetric strain is measured as $\epsilon_V = (V_0 - V_i)/V_0$, where V_0 and V_i are the volume of the binary filled image at the initial and deformed state, respectively.

Strain fields inside the specimen are computed directly from the results of particles tracking. For this, the particles displacements obtained for each scan are projected onto a regularly spaced grid, similar to the approach used in [29]. The size of the mesh is set at 10 voxels (compared to the lentil mean large axis of 15 voxels), and corresponds to the edge of a cube with the same volume as the mean volume of the tetrahedra of a Delaunay tessellation over the particle centres. The latter is taken as a reliable representation of the internal arrangement of particles, suitable for defining and computing strains in granular materials as in [30]. For each quadrilateral element (Q8) of the mesh, a transformation gradient tensor is computed at the centre of the element, using the displacement vectors of the corresponding nodes. The maximum deviatoric and volumetric strains of the Q8 element are then computed with ease, using the right stretch tensor obtained through a polar decomposition of the transformation gradient tensor.

As for interparticle contacts, identifying them in x-ray tomography is particularly challenging due mainly to the partial-volume effect, coupled with the physical interpretation of a contact - two objects can be infinitesimally close but not necessarily in contact. The contact detection algorithm developed [18] is used, applying a global threshold to determine possible contacts and a local threshold of 0.7 (relative to the normalised greyscale histogram) to improve the detection process. A random walker algorithm is applied to establish the contact plane, and the contact normal orientation is computed through a principal component analysis on the point cloud describing the contact region. Additionally, only contacts that present more than 15 voxels within the contact region are taken into account.

2.3 Fabric

Once all particles are identified and the contacts between them are measured, the particle-based and contact-based fabric tensors are calculated using the definition of fabric tensor given by [31] as:

$$\mathbf{F} = \frac{1}{N} \sum_{k=1}^{N} \mathbf{v}^k \otimes \mathbf{v}^k \tag{1}$$

where N is the number of elements of the grain-based features used to define the fabric tensor, *i.e.*, particle orientation or contact normal direction, and $\mathbf{v}^k$ is the unit norm vector attributed to the kth feature. The contact normal fabric tensor is built using the contact orientation vectors formerly presented, while the orientation vector of each particle (as defined in Fig. 1) is used for the particle orientation fabric tensor. The degree of anisotropy of the fabric tensor is characterised by

$$\zeta = \sqrt{\frac{1}{2}((a_1 - a_2)^2 + (a_2 - a_3)^2 + (a_3 - a_1)^2)} \tag{2}$$

where a_1, a_2, a_3 are the eigenvalues of $\mathbf{F}$. The use of ζ as a measure of anisotropy is convenient to understand the plausible range of anisotropy, since $0 \leq \zeta \leq 1$. The extreme case of $\zeta = 1$ corresponds to a perfect alignment of the orientation vectors along the eigenvector of a_1 (implying $a_2 = a_3 = 0$), while an isotropic distribution is described by $\zeta = 0$.

3 Results

3.1 Macroscopic behaviour and ROI

The macroscopic response is presented in Fig. 3, with $q = \sigma_1 - \sigma_3$ and $p = \frac{1}{3}(\sigma_1 + 2\sigma_3)$, and σ_1 and σ_3 being the major and minor principal stress, respectively. The regularly spaced drops of q/p correspond to stress relaxation during the stages at which the loading system is temporary halted for performing the x-ray scan. The images at each scan are used to measure the mean cross-sectional area (by dividing the current specimen volume by the current height). A linear interpolation is performed for points between scans, to obtain a measurement of the instantaneous area during the test from which the axial stress can be computed with ease. It can be observed that the q/p response is similar for specimens $\theta_0 = [30° - 60°]$ for overall strains up to 20%. LENGP00 presents the highest shear strength among the specimens, while LENGP90 displays the lowest values. Interestingly, near the end of test LENGP30, q/p gradually increases until reaching the same values as LENGP00. This behaviour can be understood as a result of the particles rotating, which is discussed in the following section.
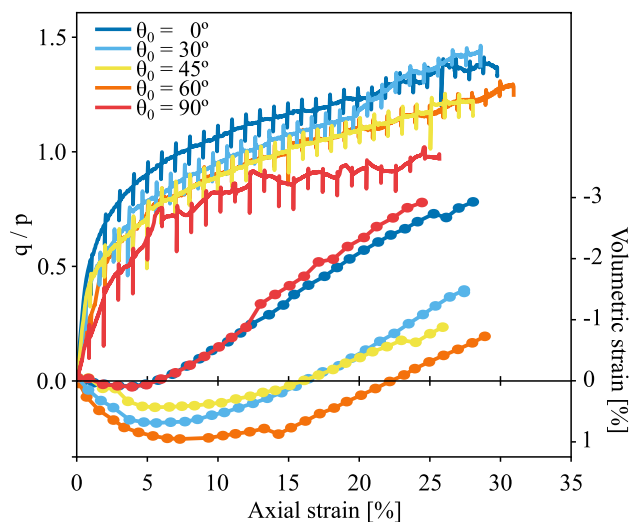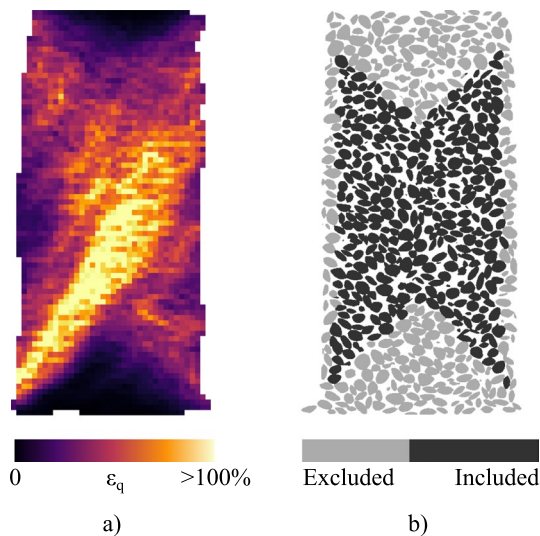

Fig. 3 Macroscopic stress-strain responses measured in the tests

The volumetric strain evolution displays an initial contracting phase followed by dilation for all the specimens. The extreme cases of $\theta_0 = 0°$ and $\theta_0 = 90°$ present a larger dilation due to a relative small contracting phase. As θ_0 increases from 0° to 60°, the response is less dilative, as observed in several existing experimental observations [2, 4, 6, 9–12, 14]. However, LENGP90 deviates the observed trend from all the other experiments, presenting a higher dilation than $\theta_0 = [30° - 60°]$, and a similar response as LENGP00.

The collection of labelled images, coupled with the tracking results, provides a unique opportunity to perform a grain-based analysis over the experimental data. However, if the entire set of particles is used, the average measured response is affected by the boundary conditions, as shown in [32]. Specifically, the spatial arrangement of particles in contact with the membrane is dominated by the latter, rather than on the interaction with their neighbours, or the specimen preparation method. This generates not only a difference between the local void ratio near the membrane and the one measured in the core of the specimen, but also a difference between the orientation of the particles, that tend to be parallel to the membrane when in contact with it. This is easily solved by excluding the peripheral layer of particles from the region to study, as presented in [33, 34]. Additionally, a second boundary effect is observed due to the restriction of the degrees of freedom of the lower end cap - allowed only to displace vertically. Figure 4a shows a vertical slice of the *total* maximum deviatoric strain field for LENGP60 at the end of the test, where a clear friction cone can be observed near the specimen ends. Given that these particles experience negligible deformation, including them

in the region of study will have a negative impact over the average measured response. For this reason, the region of interest in this study excludes the particles on the perimeter of the specimen, as well as the ones located within the static cones, as shown in Fig. 4b.

3.2 Grain kinematics

The evolution of particle and contact orientation is used as a first-order metric to quantify the internal reorganisation of the specimens under deviatoric load. To better understand the transformation of the contact and particle network, the main orientation vector of each of these two vectorial distributions is computed as $\bar{x} = \frac{1}{n}\sum_i^n x_i$ [35], and decomposed into (α, θ) as per Fig. 1. Figure 5a presents the change of the azimuth α_i relative to the initial value α_0 for specimens LENGP30 to LENGP90, for both contacts (α_C) and particles (α_P). Specimen LENGP00 is excluded since the azimuth for $\theta = 0°$ is not defined. Remarkably, for all specimens the
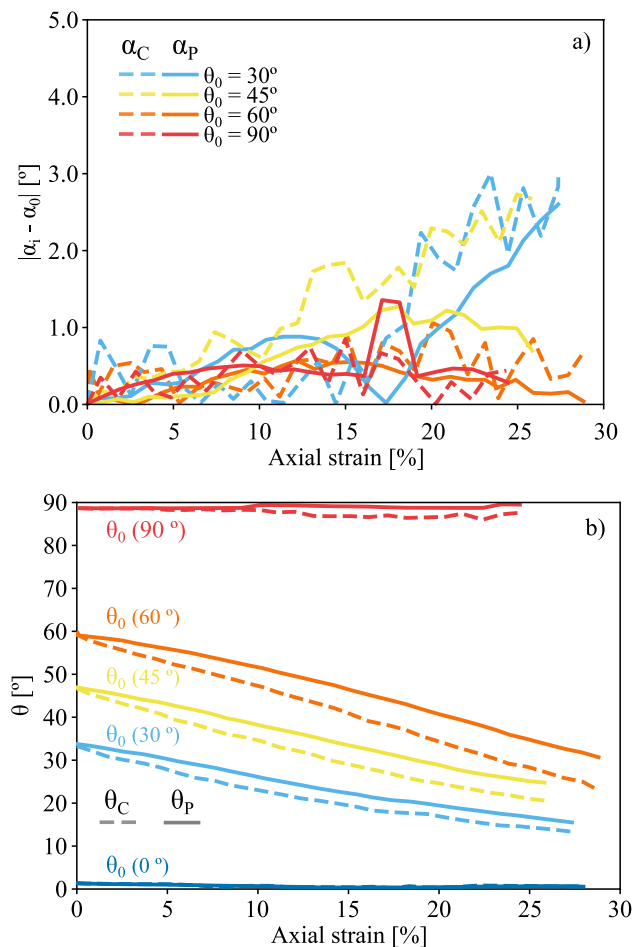
Fig. 4 Definition of regions to be taken into account in this study: **a** vertical slice of deviatoric strain at the end of the test for LENGP60; **b** Particles inside the region of interest (dark grey), and excluded particles (light grey)

Fig. 5 Evolution of particle (continuous line) and contact (dashed line) orientation expressed as: a) an absolute variation of azimuth (α), and b) variation of inclination (θ)

maximum variation of α (for both contacts α_C and particles α_P) is below 4°, and the behaviour is also observed for the rotation of individual particles. This result is *a priori* unexpected, since the deformation process induced by the deviatoric load may generate a random (or axisymetric) rotation of the particles with respect to α_0. On the contrary, the initial azimuth is almost preserved during the test. This major result incidentally simplifies the analysis of the internal deformation processes of the specimens, since the rotation of particle and contact orientation vectors can be safely characterised by only taking into account the change in inclination ($\Delta\theta$).

Figure 5b displays the evolution of inclination of the contact (θ_C) and particle (θ_P) network along the test. It can be seen that at the initial state, both networks present the same mean orientation as a result of the specimen preparation, and as the deviatoric load is increased, each subset decreases its mean orientation. An influence of inherent anisotropy on particles rotation can be observed, since for higher values of θ_0, θ_P and θ_C decrease faster. This is also observed by [10, 12], and corresponds to the greater instability against torques generated by eccentric forces. However, the mean orientation of the contact network evolves slightly faster than the mean orientation of the particles. The latter is exacerbated by the initial orientation of the specimen, since for LENGP30 the difference between the two subsets is only 1.5° at the end of the test, while for LENGP60 is almost 8°.

Although the previous observations are valid for all the specimens, LENGP90 exhibits a unique behaviour that is worth discussing. As observed in Fig. 5b, the specimen at $\theta_0 = 90°$ shows a relatively constant orientation during the entire test. Even though this results appears to be odd compared to the measurements in the other specimens, it can be explained by looking at kinematics of the particles. Figure 6a, b presents a vertical slice of a subset of LENGP90 at the initial scan and at the end of the test. Both slices are taken at an azimuth value of 0°. At the initial configuration of the specimen, the particles present an inclination near 90°, but with a slight deviation of a few degrees to either side (left or right). Interestingly, the subset at the end of the test displays a large distortion of the internal arrangement, with particles rotating either "leftwards" *or* "rightwards". This bimodal rotation emerges as a result of the small deviation of individual particles, along with the interaction with their neighbours. For all the other specimens, the particles can only rotate along one direction (creating a unimodal distribution of rotations), while the particles in LENGP90 can rotate along two directions.

Even though the visual inspection of the vertical slices provides a glimpse into the unique behaviour of LENGP90, it falls short explaining the constant orientation of θ_P and θ_C. Figure 6c–f shows the spherical histogram of the particle and contact vectors, at the beginning and end of the test.
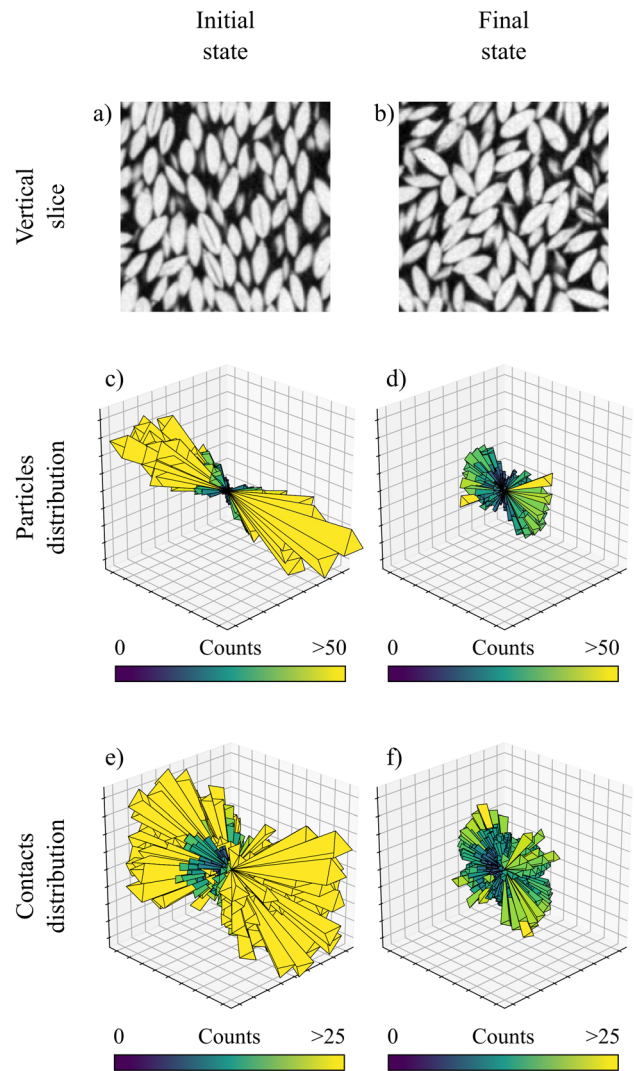
Fig. 6 Singularity of $\theta_0 = 90°$. a–b: vertical slice subset, c–d spherical histogram of particle orientation vectors, e–f spherical histogram of contact normal orientation vectors

It can be seen that both initial distributions present a clear mean orientation while presenting a difference in the spread. This can also be observed on the maximum number of counts on each histogram, pointing to the higher concentration of the particles orientation distribution. Both histograms are presented with a different scale to ease the visualisation of the main orientation and the spread. At the last scan the distribution of particles decreases its radius, implying a reduction on the maximum number of counts, while the spread increases. However, the main orientation of the distribution is kept unchanged. In the case of contacts, the distribution decreases its concentration while preserving its main direction, displaying a X-plane. The fact that in both distributions the main direction is preserved reveals that particles are rotating in both directions with equal probability.

For this reason, the relative unvariant evolution of θ_C and θ_P measured for LENGP90 is the result of the symmetrical rotation of particles in opposite directions, preserving the main orientation but increasing the spread of each distribution.

3.3 Fabric

The use of a fabric tensor provides a better understanding of the internal structure of the granular assembly and its evolution, rather than just the mean orientation of the assembly. Figure 7a presents the scalar anisotropy (computed through Equation 2) of the particle-based (ζ_P) and contact-based fabric (ζ_C) as a function of axial shortening. Once again, the initial values of ζ are similar for all the specimens, pointing to the replicability of the specimen preparation method in terms of the internal organisation of the particles. Contrary to the other tests, during the preparation of the LENGP90 specimen the membrane (and the mould) are parallel to the plane of the symetry of the particles, resulting in a positive feedback between them, increasing the overall anisotropy of the granular assembly. As expected, the initial anisotropy of the contact-based fabric is smaller than the one observed for the particles-based fabric. This is due to the isostasticity required on the contact network, thus contacts are always present in a wider set of orientations. Particles, on the other hand, can be organised even in a "perfect" distribution - where all the orientation vectors are pointing in the same direction. As deviatoric load is applied, ζ_C and ζ_P start to increase for specimens $\theta_0 = [0° - 60°]$, implying that as the particles rotate, both distributions (contact and particle network) become more concentrated along the evolving mean orientation. LENGP90, contrary to all the other specimens, decreases its scalar anisotropy (for both fabric tensors) during the test. As previously observed, the dramatic decrease of ζ is due to the bimodal rotation of the particles that disturb the local arrangement, as seen in Fig. 6b. Additionally, there is a clear effect of inherent anisotropy on the evolution of ζ: as θ_0 decreases, the rate of variation of ζ increases for both fabric tensors. Along with the results of the previous section, it can be stated that under deviatoric loading, the fabric of an inherently anisotropic material undergoes two main transformations: i) rotation of the principal direction of contacts and particles towards the direction of the major principal stress, and ii) increase of the concentration of the distribution. For higher values of θ_0, the rotation of the fabric tensor is the dominant mechanism, while for specimens with values of θ_0 closer to the direction of the principal stress, the increase of concentration is the dominating process. For intermediate values (as LENGP30 and LENGP45), both mechanisms are active at the same time.

As seen from the previous results, the particle-based fabric and contact-based fabric are interlinked, in this case by the shape of the particles. Given that all the tests were
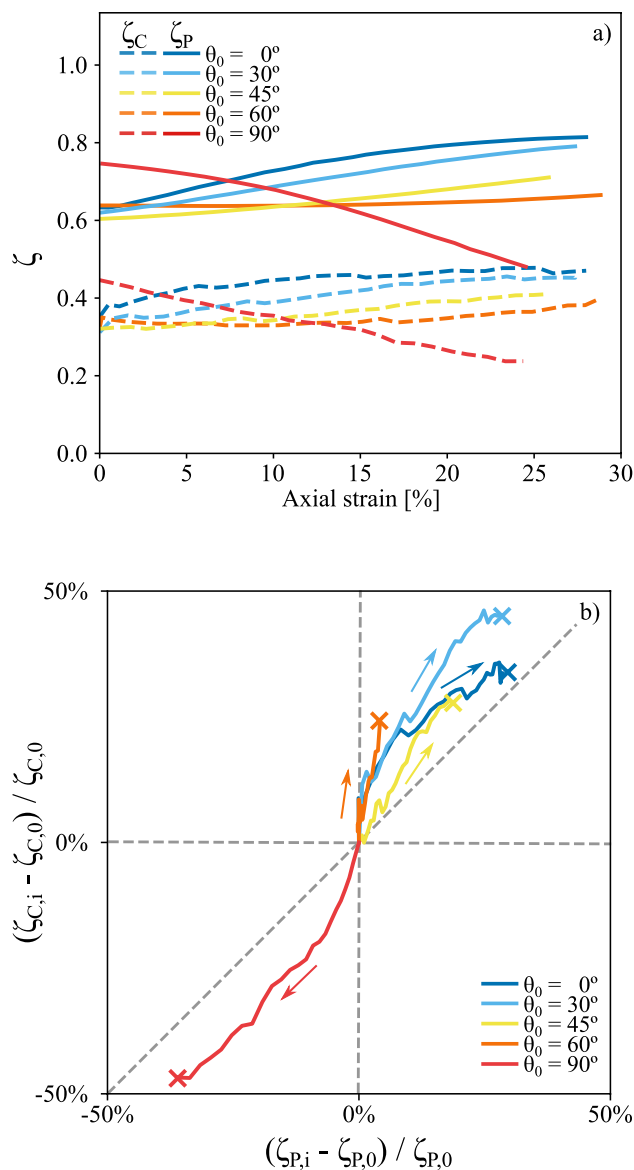
Fig. 7 Fabric evolution: **a** anisotropy of particle-based (ζ_P) and contact-based fabric (ζ_C) as a function of axial shortening, **b** Normalised variation of both fabrics relative to their initial value. The cross marks the end of the test

performed under the same experimental conditions, it can be expected that the relation between the two fabric tensors is unique and independent from the inherent anisotropy. Figure 7b presents the normalised evolution of ζ_C and ζ_P, relative to their initial value. If the relation between the two fabric tensors is invariant with respect to θ_0, all the curves should collapse on the same path. However, this is not the case. For all tests, the contact-based fabric evolves faster than its particles counterpart, while the rate $\Delta\zeta_C/\Delta\zeta_P$ differs from one test to another. This representation also provides an opportunity to visualise how the two fabric evolution mechanisms presented above evolve through the test. In the case of

LENGP60, ζ_P increases very slowly compared to ζ_C, revealing that in the particle-based fabric the only active mechanism is the rotation of the tensor - while for the contact-based fabric both mechanisms are active. On the other hand, LENGP00 displays a ratio $\Delta\zeta_C/\Delta\zeta_P \approx 1$ at the end of the test (marked by a cross), along with an important variation of both fabric anisotropies. This indicates that the overall rotation of the fabric tensor is diminished, and the dominant mechanism is the increase of the concentration around the mean orientation. LENGP45 and LENGP30 present intermediate scenarios, where both mechanisms are active at the same time. However, the higher variation of anisotropy observed on LENGP30 points to the larger role of the concentration mechanism on this specimen. Finally LENGP90 shows a decrease on both anisotropies as expected, yet it can be seen that ζ_C decreases faster than ζ_P. Additionally, the evolution is similar to the one measured for LENGP30 and LENGP00 (although on the negative quadrant of the $\Delta\zeta_C/\Delta\zeta_P$ space), where the active mechanism is the change of concentration around the mean orientation rather than the rotation of the fabric tensor.

3.4 Strain localisation

For the analyses presented above the underlying assumption is that the deformation process inside the ROI is similar for all the specimens. This can easily be verified by using the incremental displacement field (between two consecutive scans), and computing an incremental strain field, as presented in Sect. 2.2. Figure 8 shows vertical slices of the incremental maximum deviatoric strain field at the three instants during the test (beginning, midpoint, and near the end). The increment is taken at the same axial strain level for all the specimens, and the strain field is divided by the length of the overall axial strain increment.

It can be seen that at the early stages of the test, the deformation is characterised by a diffuse pattern located along the middle section of the specimens. The two rigid cones, due to friction at the specimen ends and characterised by almost no deformation, are easily visible. At a mesoscopic level, multiple deformation mechanisms parallel to each other are active, presenting an orientation around two main (and conjugate) directions. At the midpoint of the test, the number of active mechanisms decreases, possibly due to the confluence of two mechanisms that come close together, while the magnitude of the incremental deviatoric strain increases. Strain localisation, starts to manifest for some specimens at this stage. While LENGP60 displays a strong principal shear band (running from the lower-left to the upper-right corner), LENGP90 shows two main active - and conjugate - shear bands.

Until this strain level, it could be said that the deformation patterns observed are rather indifferent to θ_0. However, in
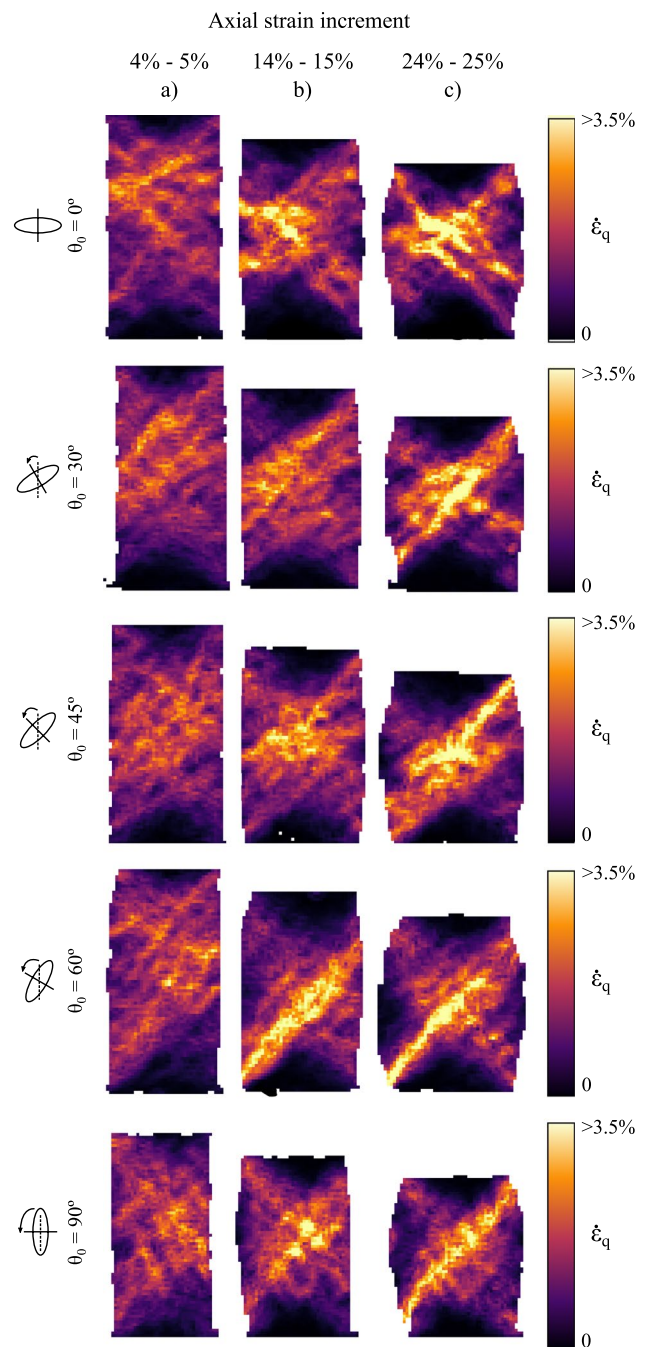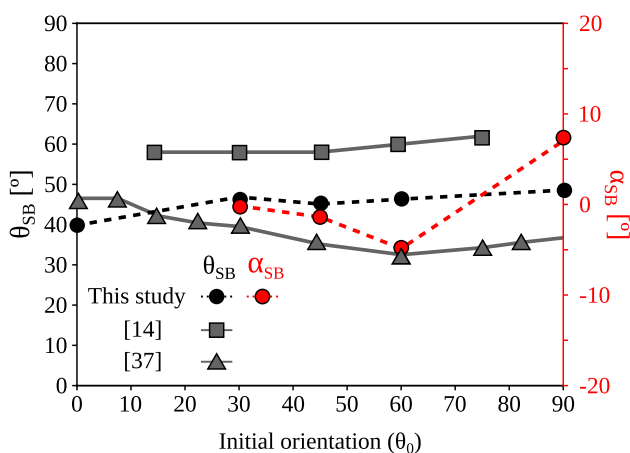

Fig. 8 Incremental deviatoric strain fields at different strain increments during the test

the final part of the test, some differences emerge between the specimens. In a broad sense, the local deformation takes place as a principal shear band (named Type-B in [8, 9, 15]), concentrating higher values of deviatoric strain, together with a secondary conjugate shear band with intermediate values (named Type-A in [8, 9, 15]). This cross-pattern deformation arises as a kinematic requirement to the DOF of the end caps, as shown by [15, 36]. The interplay between

these two shear bands is different among the specimens: while LENGP00 and LENGP30 exhibit two competitive and conjugate shear bands acting at in the same strain increment; LENGP60 and LENGP90 show a very dominant principal shear band, accompanied by a diffuse (but visible) secondary shear band, doubtlessly originated from kinematic compatibility; and LENGP45 displays only a principal shear band, where the secondary is almost non-existent. Additionally, the morphology of the principal shear band itself shows dissimilarities. While for LENGP60 and LENG90 it is highly concentrated and narrow, LENGP45 presents a very wide shear band. On the other hand, LENGP00 and LENGP30 manifest a rather diffuse (but still perceptible) principal shear band.

Figure 9 presents the results of the orientation of the principal shear band in terms of azimuth (α_{SB}) and inclination (θ_{SB}), for the last increment of each test, computed through a singular value decomposition analysis of the region corresponding to high values of deviatoric strain. The values of α_{SB} reported are measured relative to the mean initial azimuth of the particles. It can be seen that the variation of the azimuth - for the specimens where the azimuth can be computed - is close to 0°, with the exception of LENGP90 where a minor variation of 7° can be observed. The latter can be explained due to the more complex pattern of strain localization with a narrower principal shear band and lower incremental deviatoric strains, making the computation of α_{SB} more sensitive to local effects. The almost no-variation of α_{SB} with respect to the mean initial azimuth of the particles is a consequence of the strong role of the particles shape and the existence of inherent anisotropy within the specimen, leading to the development of a planar deformation process under deviatoric loading. It shows that, not only the kinematics at the microscale (*i.e.*, particle rotation) take place essentially under a 2D constraint (as shown in Sec. 3.2), but

also the deformation patterns at the mesoscale (*i.e.*, shear bands) can be understood as an essentially planar scenario. Regarding the inclination of the shear band (θ_{SB}), it can be thought that its value is affected by the initial orientation of the particles (θ_0), since this plane can be presumed to be a structural imperfection, forcing the deformation to take place along this preferential direction. However, the behaviour observed reveals that the values of θ_{SB} are always very close to 45°, disregarding the initial and final mean inclination of the particles within the region studied. This is in agreement with the trends observed by [14] and [37], obtained through 2D DEM simulations on specimens with inherent anisotropy, presented in Fig. 9. It is important to note the differences in the experimental conditions of each study. While [14] used elliptical particles with an aspect ratio of 3.3 and inherent anisotropy was achieved by means similar to the present study, [37] used spheres and represented the effect of inherent anisotropy by applying a rotation of the coordinate system of the deformation gradient imposed on the boundaries of the elementary volume. Independently of the major microstructural differences between the studies, the inclination of the shear band remains indifferent to the initial orientation of the particles. This implies that the orientation of the principal shear band does not emerge by pre-existing "fault" planes inside the specimen, but rather as a function of the properties of the material (e.g., interparticle friction angle, dilatancy angle), as suggested by the Coulomb and Roscoe rupture plane solutions. Although it can be thought that the inclination of the shear band may be affected by the initial value of anisotropy, recent work done by [15] showed numerically that the inclination of the shear band of a specimen with "randomly" oriented particles is similar to the one obtained when testing a specimen with all particles initially inclined at $\theta_0 = 45°$, strengthening the idea that the orientation arises as a consequence of the material properties.

4 Summary and outlook

The deposition of particles under the action of gravity in natural soils, induces a structural anisotropy, specially for anisometric particles. The study of this effect of initial fabric and its evolution is of utmost importance to fully understand the relation between the micro-behaviour and the macro-response of granular materials. In the present paper, five triaxial compression tests were performed over lentil specimens with a preferential initial orientation (θ_0). The unique specimen preparation method employed enables the preparation of specimens where all the particles present a similar inclination angle, reproducing the bedding effect of natural soil deposition, under controlled and reproducible conditions. The tests were performed using x-ray tomography to image the specimens at multiple stages.

Fig. 9 Orientation of the principal shear band in terms of inclination (θ_{SB}) and azimuth (α_{SB}) at the last scan

Although the experiments and analysis are fully 3D, the results show that the deformation process at the micro and mesoscale takes place essentially as a 2D process. At the particle scale, the azimuth angle (α) presents almost no variation during the rotation of the particles, easing the description of the grain kinematics by evaluating only the evolution of the inclination angle (θ). As a result, the shear bands observed at the end of the test also exhibit a value of α near $0°$, regardless of the initial value of θ_0. This result implies that, for the given aspect ratio of the studied ellipsoids, the deformation process at any scale can be understood under a planar scenario. This facilitates the development of future studies (experimental and numerical) in inherently anisotropy under a 2D assumption, describing the same phenomena as in a 3D test. The particle-based and contact normal-based fabric is measured from the labelled and greyscale images of each scan, respectively, revealing that fabric of inherently anisotropic materials evolves through two main mechanisms: *i*): rotation of the main orientation of the fabric tensor, and *ii*): increase of its anisotropy. At any instant along the test, the inclination of the particles dictates the relative importance of each mechanism: for assemblies where the particles have an inclination closer to $\theta=0°$, the second mechanism is the predominant process, while the rotation of the fabric tensor dominates the evolution of fabric for particles assemblies with an orientation further away from $\theta=0°$. Most importantly, the results reveal that fabric evolution must be understood in the context of main orientation and anisotropy, since both mechanisms are always present during deviatoric loading. Regarding the orientation of the principal shear band, it was observed that its inclination does not coincide with a "weak plane" generated due to the initial orientation of the specimen. This result is in agreement with previous studies, with different experimental conditions and particle characteristics, pointing to the fact that the inclination of the shear band depends on the properties of the granular material, and not on the structural characteristics of the specimen.

Additionally, the measurements presented in this study can be used for calibration of numerical models, as the one in [38] for the evolution of fabric tensors in inherently anisotropic granular materials. Although 9000 grains does not represent a large amount of grains for a 3D granular array, the essence of the observations presented are still valid when compared to a similar specimen with a higher number of particles. Moreover, the experimental setup introduces strong constraints on the kinematics of the system. The restricted degrees of freedom of the end caps induce the existence of complementary and conjugate shear bands, limiting the study to an averaged behaviour analysis inside the study region. A new experimental setup, that forces the creation of a unique shear band for each test, has been developed and it is currently used to study the evolution of fabric inside the shear band, understanding the origin of strain localisation and the effect of particle properties on it.

Declarations

References

1. Arthur, J., Menzies, B.: Inherent anisotropy in a sand. Geotechnique **22**(1), 115–128 (1972)
2. Oda, M.: Initial fabrics and their relations to mechanical properties of granular material. Soils Found. **12**(1), 17–36 (1972)
3. Arthur, J., Chua, K., Dunstan, T.: Induced anisotropy in a sand. Geotechnique **27**(1), 13–30 (1977)
4. Oda, M., Koishikawa, I., Higuchi, T.: Experimental study of anisotropic shear strength of sand by plane strain test. Soils Found. **18**(1), 25–38 (1978)
5. Oda, M., Konishi, J., Nemat-Nasser, S.: Experimental micromechanical evaluation of strength of granular materials: effects of particle rolling. Mech. Mater. **1**(4), 269–283 (1982)
6. Lam, W.-K., Tatsuoka, F.: Effects of initial anisotropic fabric and $_2$ on strength and deformation characteristics of sand. Soils Found. **28**(1), 89–106 (1988)
7. Yoshimine, M., Ishihara, K., Vargas, W.: Effects of principal stress direction and intermediate principal stress on undrained shear behavior of sand. Soils Found. **38**(3), 179–188 (1998)
8. Tatsuoka, F., Sakamoto, M., Kawamura, T., Fukushima, S.: Strength and deformation characteristics of sand in plane strain compression at extremely low pressures. Soils Found. **26**(1), 65–84 (1986)
9. Tatsuoka, F., Nakamura, S., Huang, C., Tani, K.: Strength anisotropy and shear band direction in plane strain tests of sand. Soils Found. **30**(1), 35–54 (1990)

10. Mahmood, Z., Iwashita, K.: Influence of inherent anisotropy on mechanical behavior of granular materials based on DEM simulations. Int. J. Numer. Anal. Methods Geomech. **34**(8), 795–819 (2010)

11. Sazzad, M.M., Suzuki, K.: Micromechanical behavior of granular materials with inherent anisotropy under cyclic loading using 2d DEM. Granular Matter **12**(6), 597–605 (2010)

12. Hosseininia, E.S.: Investigating the micromechanical evolutions within inherently anisotropic granular materials using discrete element method. Granular Matter **14**(4), 483–503 (2012)

13. Fu, P., Dafalias, Y.F.: Fabric evolution within shear bands of granular materials and its relation to critical state theory. Int. J. Numer. Anal. Methods Geomech. **35**(18), 1918–1948 (2011)

14. Fu, P., Dafalias, Y.F.: Study of anisotropic shear strength of granular materials using DEM simulation. Int. J. Numer. Anal. Methods Geomech. **35**(10), 1098–1126 (2011)

15. Zhao, J., Guo, N.: The interplay between anisotropy and strain localisation in granular soils: a multiscale insight. Géotechnique **65**(8), 642–656 (2015)

16. Wang, R., Cao, W., Zhang, J.-M.: Dependency of dilatancy ratio on fabric anisotropy in granular materials. J. Eng. Mech. **145**(10), 04019076 (2019)

17. Li, X.S., Dafalias, Y.F.: Anisotropic critical state theory: role of fabric. J. Eng. Mech. **138**(3), 263–275 (2012)

18. Wiebicke, M., Andò, E., Herle, I., Viggiani, G.: On the metrology of interparticle contacts in sand from x-ray tomography images. Meas. Sci. Technol. **28**(12), 124007 (2017)

19. Pinzón, G., Andò, E., Desrues, J., Viggiani, G.: Fabric evolution and strain localisation in inherently anisotropic specimens of anisometric particles under triaxial compression, 2021. Available at https://zenodo.org/record/5744160

20. Yuan, Y., Jiao, Y., Wang, Y., Li, S.: Universality of jammed frictional packing. Phys. Rev. Res. **3**(3), 033084 (2021)

21. Stamati, O., et al.: Spam: software for practical analysis of materials. J. Open Source Softw. **5**(51), 2286 (2020)

22. Vincent, L.: Morphological grayscale reconstruction in image analysis: applications and efficient algorithms. IEEE Trans. Image Process. **2**(2), 176–201 (1993)

23. Tengattini, A., Andò, E.: Kalisphera: an analytical tool to reproduce the partial volume effect of spheres imaged in 3d. Meas. Sci. Technol. **26**(9), 095606 (2015)

24. Hall, S.A., Bornert, M., Desrues, J., Pannier, Y., Lenoir, N., Viggiani, G., Bésuelle, P.: Discrete and continuum analysis of localised deformation in sand using x-ray μCT and volumetric digital image correlation. Géotechnique **60**(5), 315–322 (2010)

25. Andò, E., Hall, S.A., Viggiani, G., Desrues, J., Bésuelle, P.: Grain-scale experimental investigation of localised deformation in sand: a discrete particle tracking approach. Acta Geotech. **7**(1), 1–13 (2012)

26. Andò, E., Dijkstra, J., Roubin, E., Dano, C., Boller, E.: A peek into the origin of creep in sand. Granular Matter **21**(1), 11 (2019)

27. Pinzón, G., Andò, E., Tengattini, A., Viggiani, G., Desrues, J.: Contact evolution in granular materials with inherently anisotropic fabric, in EPJ Web of Conferences, vol. 249, p. 06015, EDP Sciences, 2021

28. Andò, E.: Experimental investigation of microstructural changes in deforming granular media using x-ray tomography. PhD thesis, Université de Grenoble, 2013

29. Desrues, J., Viggiani, G.: Strain localization in sand: an overview of the experimental results obtained in grenoble using stereophotogrammetry. Int. J. Numer. Anal. Methods Geomech. **28**(4), 279–321 (2004)

30. Bagi, K.: Stress and strain in granular assemblies. Mech. Mater. **22**(3), 165–177 (1996)

31. Nadler, B., Guillard, F., Einav, I.: Kinematic model of transient shape-induced anisotropy in dense granular flow. Phys. Rev. Lett. **120**(19), 198003 (2018)

32. Jerkins, M., Schröter, M., Swinney, H.L., Senden, T.J., Saadatfar, M., Aste, T.: Onset of mechanical stability in random packings of frictional spheres. Phys. Rev. Lett. **101**(1), 018301 (2008)

33. Schaller, F.M., Neudecker, M., Saadatfar, M., Delaney, G.W., Schröder-Turk, G.E., Schröter, M.: Local origin of global contact numbers in frictional ellipsoid packings. Phys. Rev. Lett. **114**(15), 158001 (2015)

34. Schaller, F.M., Kapfer, S.C., Hilton, J.E., Cleary, P.W., Mecke, K., De Michele, C., Schilling, T., Saadatfar, M., Schröter, M., Delaney, G.W., et al.: Non-universal voronoi cell shapes in amorphous ellipsoid packs. EPL **111**(2), 24002 (2015)

35. Mardia, K.V., Jupp, P.E.: Directional statistics, vol. 494. Wiley, New York (2009)

36. Wu, K., Sun, W., Liu, S., Zhang, X.: Study of shear behavior of granular materials by 3d DEM simulation of the triaxial test in the membrane boundary condition. Adv. Powder Technol. **32**(4), 1145–1156 (2021)

37. Couture, C.-B.: Mechanical characterization of porous sandstones in true triaxial conditions: diffuse and localized deformation, effect of anisotropy. PhD thesis, Université Grenoble Alpes, 2020

38. Wang, R., Pinzón, G., Andò, E., Viggiani, G.: Modeling combined fabric evolution in an anisometric granular material driven by particle-scale x-ray measurements. J. Eng. Mech. **148**(1), 04021120 (2022)